Full Length Article

Effect of the ferrite morphology on hydrogen embrittlement of MAG welded 304 austenitic stainless steel

Chilou Zhou [a,*], Pengzhi Dai [a], Hao Wu [a,*], Mohan He [a], Xianhui Liu [a], Paul K. Chu [b]

[a] School of Mechanical and Automotive Engineering, South China University of Technology, Guangzhou 510641, PR China
[b] Department of Physics, Department of Materials Science and Engineering, and Department of Biomedical Engineering, City University of Hong Kong, Tat Chee Avenue, Kowloon, Hong Kong, China

A B S T R A C T

Ferrite usually plays an important role in the hydrogen embrittlement (HE) of austenitic stainless steel (γ-SS) weld. However, there are few investigations on the effect of ferrite morphology on HE. In this study, the relationship between the ferrite morphology and HE of metal active gas (MAG) welded 304 austenitic stainless steel is investigated. Hydrogen distribution testing and simulation reveal that the ferrite/austenite interfaces become the hydrogen segregation regions and the degree of hydrogen segregation at the interface is affected by ferrite morphology, which shows the order of lathy ferrite > reticular ferrite > skeletal ferrite. The slow strain rate tensile (SSRT) test indicates that the susceptibility to HE of welds containing lathy ferrite, skeletal ferrite and reticular ferrite reaches 34.6%, 30.7% and 33.2%, respectively. It can be found that the HE resistance shows the order of skeletal ferrite > reticular ferrite > lathy ferrite, which corresponds to the order of increasing hydrogen segregation. Hence, the ferrite morphology influences the resistance to HE of welds by affecting hydrogen segregation at the ferrite/austenite interface. A similar ferrite morphological dependence is observed from the weld fractures.

1. Introduction

Hydrogen with natural abundance is attractive as a renewable and pollution-free energy source to combat environmental problems arising from the combustion of fossil fuels [1–5]. However, hydrogen embrittlement (HE) of materials poses practical challenge and can cause industrial accidents. It usually leads to a severe loss of strength and ductility of the stainless steel, resulting in a significant reduction of the service life of stainless steel. Owing to the excellent mechanical properties and the high resistance to HE [6], austenitic stainless steel (γ-SS) has good prospects in high-pressure hydrogen storage [7–10]. γ-SS often needs to be supplemented by welding to meet the manufacturing requirements of components [11,12] due to needs to form complex and large structures. Studies have shown that γ-SS has excellent weldability and can be processed using different types of welding process, e.g., metal inert gas welding (MIG) [13], Keyhole tungsten inert gas welding (K-TIG) [14], laser-arc hybrid welding (LAHW) [15], laser beam welding [16], electron beam welding (EB) [17] and plasma arc welding (PAW) [18], etc. Unfortunately, the thermal cycle caused by welding promotes the formation of ferrite in welds consequently degrading the mechanical

properties and exacerbating HE [19–21]. This phenomenon is primarily caused by the different behavior of hydrogen in austenite and ferrite [22]. Although many theories such as hydrogen-enhanced decohesion (HEDE) [23], hydrogen-enhanced localized plasticity (HELP) [24] and adsorption-induced dislocation emission (AIDE) [25] have been reported to explore the long-standing problem of HE, a full understanding of the HE phenomenon of γ-SS weld has not yet been achieved. Younes et al. [17] have noted that the frequency and severity of microcracking are greater in the TIG weld than its EB counterpart due to the higher ferrite content of the former. Luppo et al. [26] have found that a larger amount of ferrite increases the susceptibility to HE of γ-SS. On the other hand, Tsay et al. [18] have reported that ferrite has no significant effect on HE in type 304 weld metal. Brooks et al. [27] have studied the effect of hydrogen on the tensile behavior in type 304L and 309S γ-SS welds and concluded that ferrite contents from 1% to 10% do not affect HE. These previous studies have focused on the effect of the ferrite content on HE but in practice, the ferrite morphology caused by different welding parameters [28] can also affect the hydrogen distribution and HE of welds. Unfortunately, the hydrogen distribution in ferrite with different morphologies and relationship between ferrite morphology

---

and HE are still not well understood.

In this study, the hydrogen distribution in electrochemical hydrogen-charged type 304 γ-SS welds is investigated using scanning Kelvin probe force microscopy (SKPFM) and magnetic force microscopy (MFM). The change in the hydrogen distributions is simulated by the finite element method (FEM). The susceptibility to HE of welds is evaluated by slow strain rate tensile (SSRT) test. Metallographic microscopy and field-emission scanning electron microscopy (SEM) are performed to characterize the microstructures and fracture morphology. Based on the difference in the hydrogen distribution, macroscopic mechanical property and hydrogen-induced fracture morphology, the effect of the ferrite morphology on the hydrogen distribution is discussed and the relationship between the ferrite morphology and HE is revealed.

2. Experimental details

2.1. Material and specimen preparation

The metal used in this study was type 304 γ-SS and the welding wire used was type E308 γ-SS. The chemical compositions of them are shown in Table 1. The γ-SS plate with thickness of 3 mm and the welding wire with diameter of 1.2 mm were used for welding. Metal active gas arc welding (MAG) was carried out using the welding machine (NB-500, Beijing Time Technologies Co., Ltd., China). The welding process was in semi-automatic mode, where the movement of the welding heat source was done by manual operation and the wire feeding and gas feeding were done by the corresponding mechanical devices. A V-groove method with the angle of 60° and the root gap of 1 mm was used so that the welding process could be done in one pass to ensure full weld penetration. The wire extension was 12 mm and the welding wire feed rate was automatically matched by the welding power source according to the welding current. A shielding gas mixture of Ar + 20% CO$_2$ setting at 10 L/min was used. Test pieces were welded using a ceramic backing without backing gas. Before welding, all the edges of the base metal were polished and cleaned so as to eschew any source of impurity like dust, rust and oxidation film, etc. Table 2 provides a detailed list of the welding parameters used in this study. The welding heat input was calculated according to the following equation:

$$HI = \frac{U \times I \times \eta}{v} \tag{1}$$

where HI represents the heat input in J/cm, U represents the arc voltage in volts (V), I represents the welding current in amperes (A), η represents the thermal efficiency coefficient and v represents the welding speed in cm/s. η of MAG is taken as 0.8 [29–33].

After welding, the joints were subjected to non-destructive testing using visual testing (VT) and X-ray radiographic testing (RT). The views of the welded joint are shown in Fig. 1, it can be found that excellent gas protection had formed during the welding process reflected by the weld color. No surface defects were observed. RT had been conducted to detect internal defects of welds. Positive results of RT were found for all joints.

The specimens for metallographic assessment and SKPFM were cut into square sheets with dimensions of 10 mm × 10 mm × 1 mm. As shown in Fig. 2, the specimens for the tensile test with a gauge length of 15 mm, gauge width of 2 mm and thickness of 2 mm were cut from the weldments and the weld was located in the middle of the specimen

Table 2
Welding parameters of MAG.

Weld	Welding current (A)	Arc voltage (V)	Welding speed (cm/min)	Heat input (kJ/cm)
M1	180	25	35	6.2
M2	200	25	35	6.9
M3	220	25	35	7.5

gauge. After cutting, each specimen was ground with 2000 grit SiC paper and polished to 0.06 μm using an alumina polishing solution. Then specimens were then cleaned ultrasonically in ethanol for 5 min.

2.2. Hydrogen distribution

SKPFM was used to determine the hydrogen distribution by measuring the contact potential difference (CPD) [34] and MFM was performed to distinguish ferrite and austenite in the specimens. The hydrogen distribution was determined using a probe height of 100 nm and scanning frequency of 0.5 Hz. Before the test, a Vickers hardness tester was used to mark the position to ensure that the same position was examined before and after hydrogen charging. The hydrogen-charged specimens were pre-charged electrochemically in 0.2 mol/L H$_2$SO$_4$ with 3 g/L thiourea at a charging current density of 50 mA/cm^2 for 24 h.

2.3. Hydrogen distribution simulation

FE models were developed to simulate the evolution of hydrogen distribution in the γ-SS welds using the general-purpose finite element program ABAQUS 6.14. The schematic view of the investigated geometric model is shown in Fig. 3, which consists of austenite (white area) and ferrite (gray area). In order to obtain the acceptable accuracy, ferrite is established by maintaining the corresponding dimensional and morphological features. The hydrogen-related input parameters used in the simulation were taken from available literature on hydrogen diffusion in ferritic and austenitic steel [35–37] as shown in Table 3. A constant hydrogen concentration of 1 ppm was applied to the lower boundary and 0 ppm was applied on the upper boundary of the model. Therefore, the direction of the hydrogen flux is from the bottom surface to the top. The hydrogen diffusion direction is vertical (positive y-direction) and diffusion is one-dimensional. The evolution of the hydrogen distribution is monitored by the transient analysis method.

2.4. Tensile test

The mechanical properties of the specimens before and after hydrogen charging were determined by the SSRT test and the susceptibility to HE was then evaluated. The SSRT test was carried out on the universal testing machine (Instron 8802) at a strain rate of 5.5×10^{-5} /s. The ultimate tensile strength (UTS) was obtained from the stress–strain curves based on the tensile data. The total elongation (El$_t$) corresponding to the strain at failure was calculated from the data of the gauge length at failure. The reduction of area (RA) was calculated from the data of the fracture which served as the basis to evaluate the susceptibility to HE. The index of hydrogen embrittlement (RA$_{loss}$) is calculated by the following equation:

Table 1
Chemical compositions of the base metal and welding wire.

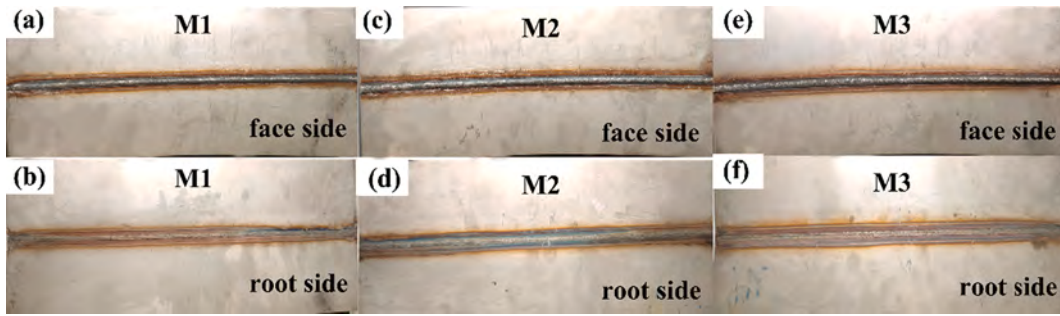| Material	C	Si	Mn	P	S	Cr	Ni	N	Fe
304 (wt. %)	0.078	0.584	1.10	0.02	0.012	19.05	8.08	0.080	Bal.
E308 (wt. %)	0.074	0.835	0.67	0.031	0.019	18.36	9.34	–	Bal.

Fig. 1. View of the welded joint: (a) Face side of M1, (b) Root side of M1, (c) Face side of M2, (d) Root side of M2, (e) Face side of M3, (f) Root side of M3.
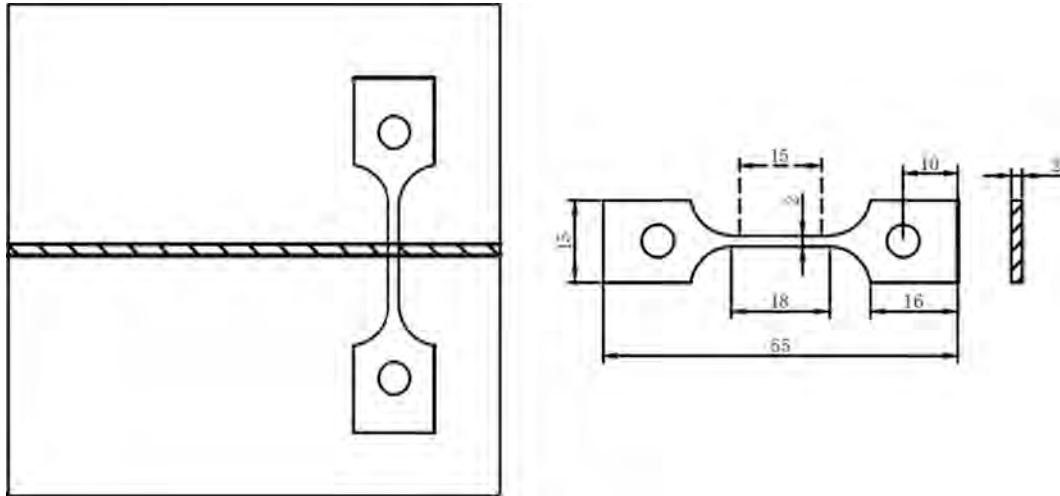

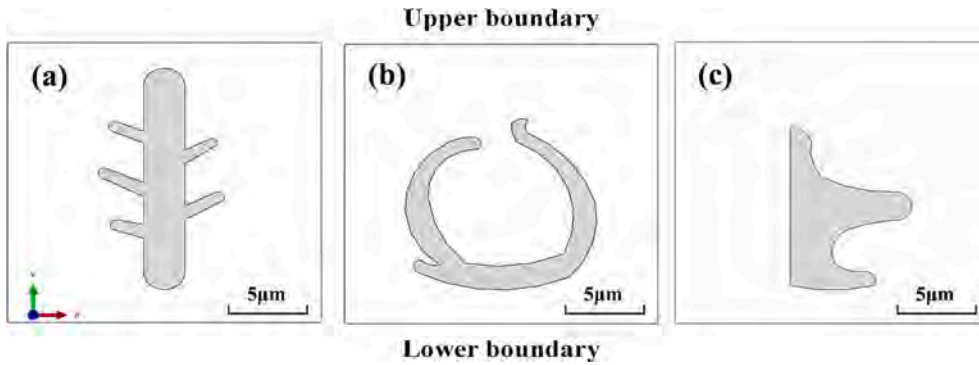**Fig. 2.** Dimensions and sampling location of tensile specimens (in mm).

Fig. 3. Schematic of geometric model: (a) Skeletal ferrite, (b) Reticular ferrite, (c) Lathy ferrite.

Table 3
Hydrogen-related input parameters for the simulation.

Phase	Diffusion coefficient (m²/s)	Solubility (ppm)
Ferrite	6.0×10^{-11} [35]	0.033 [37]
Austenite	1.4×10^{-16} [36]	32.51 [37]

$$RA_{loss} = \frac{RA_0 - RA_H}{RA_0} \times 100\% \qquad (2)$$

where RA_0 and RA_H represent the RA of the uncharged and hydrogen-charged specimens, respectively.

2.5. Characterization

Chemical composition of welds was obtained using energy spectral analyzer. The microstructure of the specimens was observed by metallographic microscope. Before observing, etching was conducted to discern the ferrite and austenite structures. A mixture of 30 mL HCL, 10 mL HNO_3 and 10 mL H_2O was used as the etching solution. Etching was carried out by a 10 s immersion in the etching solution. Then the

specimens were thoroughly rinsed using distilled water to remove residual etching solution. The fracture morphology of tensile specimens was examined by SEM.

3. Results

3.1. Microstructures

As shown in Fig. 4, the welds consist of the austenitic matrix (bright area) and ferrite (dark area) and the ferrite morphologies of M1, M2 and M3 are different as a result of the different welding parameters (in Table 2). As shown in Fig. 4(a), ferrite in M1 shows the morphology of lath. With increasing welding heat input, the ferrite morphology becomes continuous. As shown in Fig. 4(b), ferrite with the skeletal morphology is dominant in M2. Fig. 4(c) discloses zones of reticular ferrite in M3 and ferrite in M3 has mainly the skeleton and reticulation morphologies. The ferrite morphology variation can be attributed to the higher cooling rate for a low welding heat input thereby providing less time for the dendrites in ferrite to grow. On the other hand, if the welding heat input is high, the cooling rate decreases and there is more time for the dendrites in ferrite to grow giving rise to a continuous structure.

The ferrite content in each weld is determined by calculating Cr_{eq} and Ni_{eq} and then searching the WRC-1992 diagram [38] as shown in Table 4. The reason for the similar ferrite content in welds for different welding heat input is explained as follows. The ferrite content in the weld is related to the welding heat input and cooling rate after welding [39]. They show a negative correlation (higher heat input, slower cooling rate; lower heat input, faster cooling rate). When the welding heat input is low, the residence time of the weld in the temperature interval of δ-formation (initial stage of solidification process) is short, resulting in a low content of initial precipitated ferrite. The transformation of δ → γ occurs during the subsequent solidification process (cooling process). The higher cooling rate reduces the duration of the transformation of δ → γ, which retains a certain content of ferrite in the weld. When the welding heat input is higher, although a larger amount of initial precipitated ferrite has formed due to the longer residence time of the weld in temperature interval of δ-formation, the slower cooling rate prolongs the duration of the transformation of δ → γ, leading to the reduction of the initial precipitated ferrite. As a result, three kinds of welds with a similar ferrite content but different ferrite morphology are obtained.

3.2. Hydrogen distribution determined by SKPFM

The magnetic distribution map and the CPD map obtained from the same position of the weld are depicted in Fig. 5. Ferrite and austenite can be distinguished by the magnetic distribution map due to the different magnetic properties [40]. The magnetic distribution at the position marked by the red line in Fig. 5(a) is shown in Fig. 5(b) and ferrite (bright area) exhibits higher magnetic property than austenite (dark area). The CPD maps before and after hydrogen charging shown in Fig. 5 (c) and (e) reveal that the CPD of ferrite is lower than that of austenite after hydrogen charging, which is opposite to the result before hydrogen charging. This phenomenon indicates that the CPD of both ferrite and austenite increases after hydrogen charging, but the increment of austenite is greater than that of ferrite. The CPD distribution at the position marked by the red line before and after hydrogen charging is shown in Fig. 5(d) and (f) and the CPD reaches the maximum at the ferrite/austenite interface after hydrogen charging.

Our results show that lathy ferrite, skeletal ferrite and reticular ferrite are dominant in M1, M2, and M3, respectively and these three ferrite morphologies have distinct organizational characteristics. Lathy ferrite has a block and uneven structure and the length of the main axis varies from 5 to 10 μm. Skeletal ferrite has a slender and dendritic structure with obvious dendrites and the length of the main axis is generally longer than 15 μm. Reticular ferrite has a cyclic structure surrounding austenite. The CPD maps of these three morphologies of ferrite before and after hydrogen charging are displayed in Fig. 6. Since the specimens are pre-charged with hydrogen for 24 h before SKPFM, they reach the hydrogen saturation state and hydrogen is evenly distributed at the interface. Therefore, the point located at the ferrite/austenite interface (marked in Fig. 6) is investigated and the results are shown in Table 5. The CPD increment of 400 mV is found at the interface between lathy ferrite and austenite, 372 mV at the interface between skeletal ferrite and austenite, and 383 mV at the interface between reticular ferrite and austenite, indicating that the hydrogen segregation degree at the ferrite/austenite interface is affected by the ferrite morphology.

3.3. Hydrogen distribution simulated by FEM

The three ferrite morphologies observed by SKPFM are investigated by theoretical simulation. Fig. 7 reveals that the ferrite/austenite interface preferentially becomes the area of hydrogen segregation after hydrogen diffusing. Furthermore, there are obvious differences in the degree of hydrogen segregation at the interface among three different morphologies.

To intuitively show the differences in the degree of hydrogen segregation at the interface between different morphologies of ferrite and austenite, the change of the hydrogen concentration at points A and B shown in Fig. 7 is presented in Fig. 8. The results disclose that the differences in the hydrogen segregation at the interfaces between
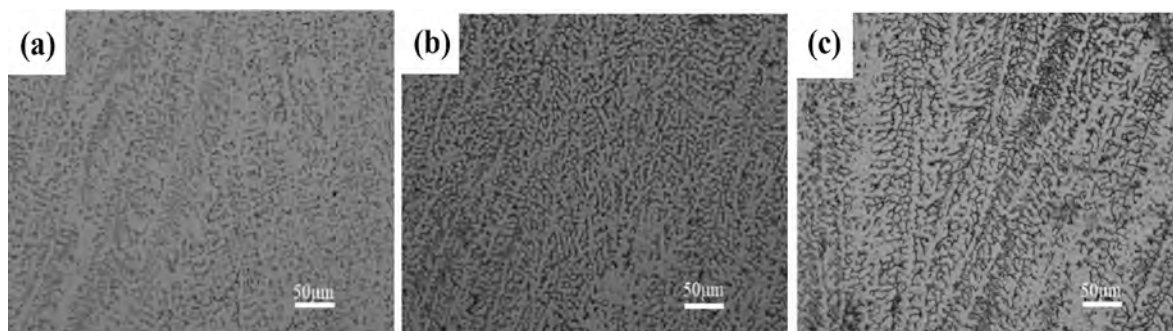
Table 4
Ferrite content in the welds for different heat input.

Specimen	Heat input (kJ/cm)	Ferrite content (%)
M1	6.2	8.2
M2	6.9	8.2
M3	7.5	8.1

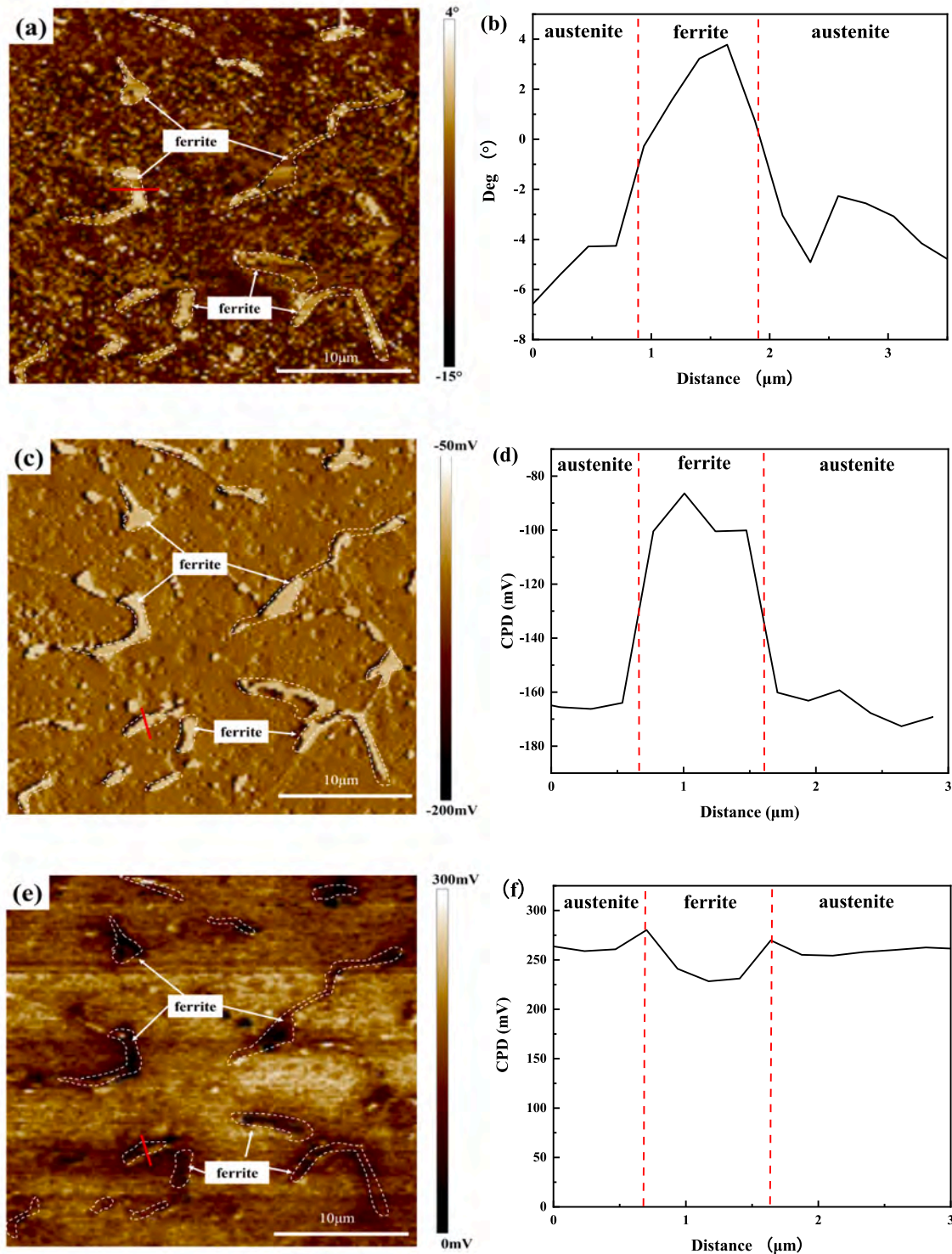**Fig. 4.** Micrographs of different welds: (a) M1, (b) M2, (c) M3.

Fig. 5. Magnetic distribution maps and CPD maps before and after hydrogen charging: (a) MFM map, (b) Magnetic property along the red line shown in (a), (c) SKPFM map of the uncharged weld, (d) CPD along the red line shown in (c), (e) SKPFM map of the hydrogen-charged weld, (f) CPD along the red line shown in (e).

different morphologies of ferrite and austenite are independent of the specific location at the interface. The hydrogen segregation degree decreases following the order of lathy ferrite, reticular ferrite, and skeletal ferrite.

3.4. Mechanical property and fracture morphology

Preliminary examination of the tensile specimens reveals that all

these specimens have fractured in the middle of the gauge, where the weld is located. The stress–strain curves of M1, M2 and M3 before and after hydrogen charging are shown in Fig. 9 and the mechanical properties are presented in Table 6. The RA_{loss} values of M1, M2 and M3 is 34.6%, 30.7% and 33.2%, respectively, indicating that welds exhibit different resistances to HE. Among the three specimens, M2 containing skeletal ferrite has the highest resistance to HE, and M1 containing lathy ferrite exhibits the highest susceptibility to HE.
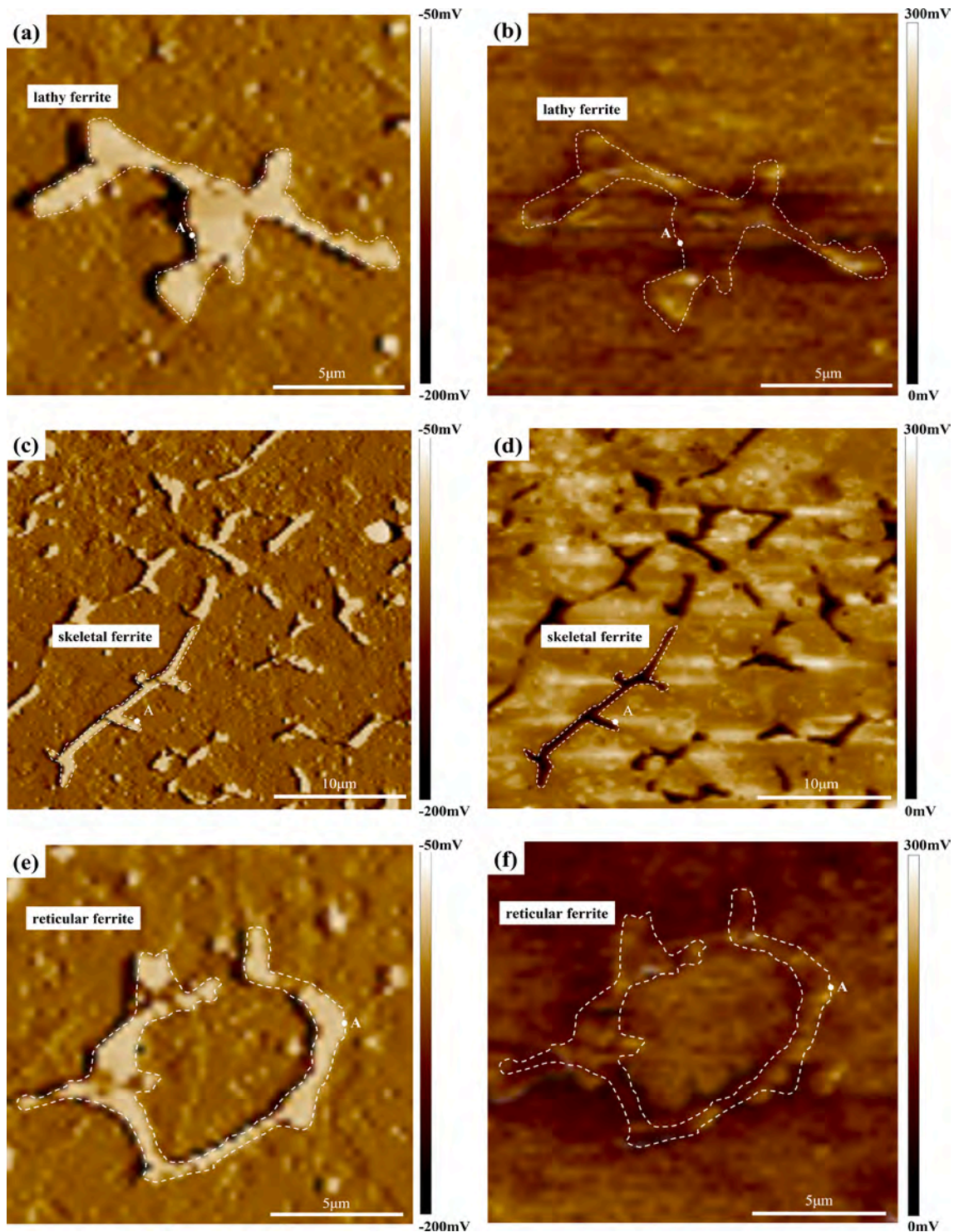
Fig. 6. CPD maps of different ferrite morphologies: (a) Lathy ferrite (uncharged), (b)Lathy ferrite (hydrogen-charged), (c) Skeletal ferrite (uncharged), (d) Skeletal ferrite (hydrogen-charged), (e) Reticular ferrite (uncharged), (f) Reticular ferrite (hydrogen-charged).

The uncharged specimens exhibit ductile fracture caused by micro-void coalescence, as shown in Fig. 10. In contrast, brittle fracture characteristics are observed from the fracture edges of the hydrogen-charged specimens. The magnified brittle areas at the edge in Fig. 11 (d), (e) and (f) reveal cleavage facets in M1 and secondary cracks and microcracks in M2 and M3. By comparing Fig. 11(a), (b) and (c), more big dimples are observed from the fracture center of M2, whereas the dimples in M1 are smaller implying that M1 has worse plasticity after hydrogen charging.

4. Discussion

According to the following calculation equation of SKPFM:

$$CPD = \frac{1}{e}\left(\varphi_{tip} - \varphi_{sample}\right) \tag{3}$$

where ϕ_{tip} and ϕ_{sample} represent the electron work function (EWF) of the tip and specimens, respectively, and e denotes the value of the elementary charge. Many studies have confirmed that hydrogen can

Table 5
CPD of the marked position.

Ferrite morphology		Figure	CPD(mV)	Δ_{CPD}(mV)
Lathy ferrite	uncharged	Fig. 6(a)	−113	400
	hydrogen-charged	Fig. 6(b)	287	
Skeletal ferrite	uncharged	Fig. 6(c)	−104	372
	hydrogen-charged	Fig. 6(d)	268	
Reticular ferrite	uncharged	Fig. 6(e)	−109	383
	hydrogen-charged	Fig. 6(f)	274	

reduce the EWF of specimen surfaces in an ultra-high vacuum environment [41,42] when the surface accuracy of specimens is relatively high. From equation (3), it can be found that the decrease of the EWF will directly lead to the increase in CPD, which demonstrates that the hydrogen segregation can be assessed by monitoring CPD.

Fig. 5 shows that the dissolution of hydrogen in austenite is greater than that in ferrite due to the different behavior of hydrogen in ferrite and austenite. In addition, the maximum CPD is observed from the ferrite/austenite interface revealing that hydrogen segregation occurs at the interface, which is supported by the simulation result in Fig. 7. The hydrogen diffusivity in ferrite is 4 to 5 orders of magnitude higher than in austenite and the hydrogen solubility in austenite is 2 to 3 orders of magnitude higher than in ferrite. Owing to the low hydrogen solubility and high hydrogen diffusivity in ferrite, ferrite can reach hydrogen saturation more quickly and act as rapid diffusion channels for

hydrogen. However, because of the high hydrogen solubility and low hydrogen diffusivity in austenite, diffusion of hydrogen is slower when passing through the ferrite/austenite interface into austenite. Hence, a large number of hydrogen atoms are dissolved and hydrogen segregation results in the interface.

From the CPD maps shown in Fig. 6 and the measurement results presented in Table 5, it can be noted that most of the hydrogen atoms accumulate at the interface between lathy ferrite and austenite, while the hydrogen segregation is the least at the interface between skeletal ferrite and austenite. This phenomenon is supported by simulation and the difference in hydrogen segregation can be explained by the ferrite morphology. Skeletal ferrite has a slender and dendritic structure with dendrites on the main axis to increase the contact area between ferrite and austenite and form more hydrogen diffusion channels. Therefore, hydrogen atoms are distributed evenly at the ferrite/austenite interface when hydrogen atoms diffuse through the interface. In comparison, reticular ferrite has a structure wrapping austenite which may cause hydrogen atoms to reenter the same reticular ferrite during diffusion after precipitating from the center area of reticular ferrite. Therefore, hydrogen segregation at the interface is promoted. Lathy ferrite has a block and uneven structure leading to a smaller contact area between lathy ferrite and austenite. During diffusion through the interface, a large number of the hydrogen atoms accumulate at the interface due to the lack of hydrogen diffusion channels.

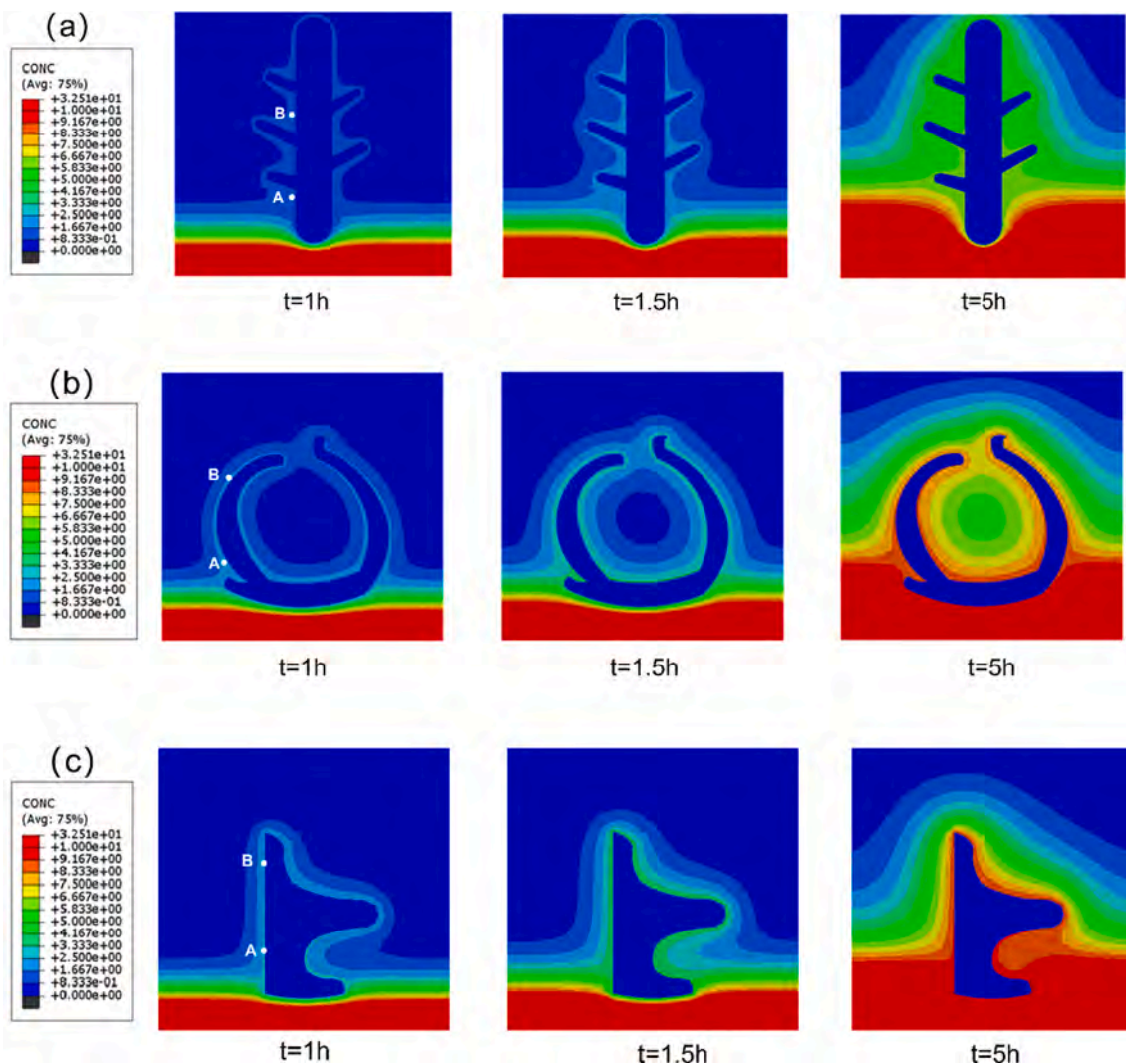M1, M2 and M3 have similar ferrite content (in Table 4) and so the

Fig. 7. Evolution of the hydrogen distribution of three ferrite morphologies: (a) Skeletal ferrite, (b) Reticular ferrite, (c) Lathy ferrite.
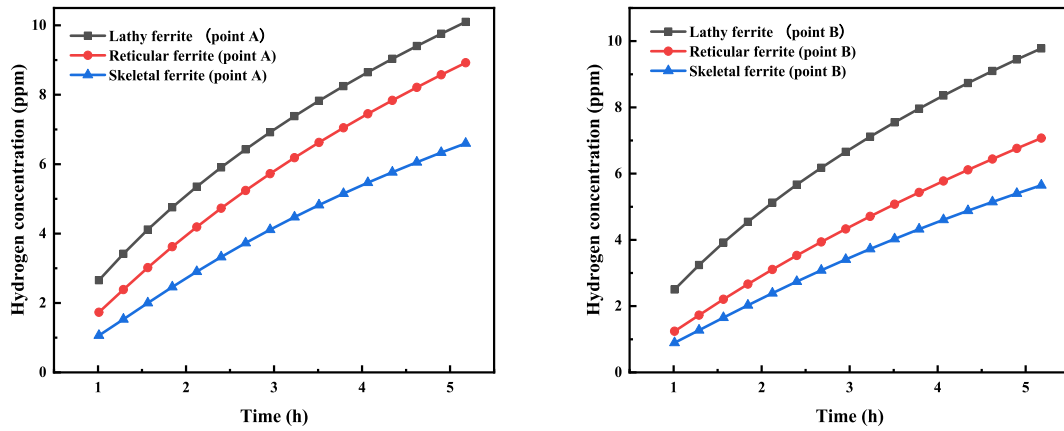
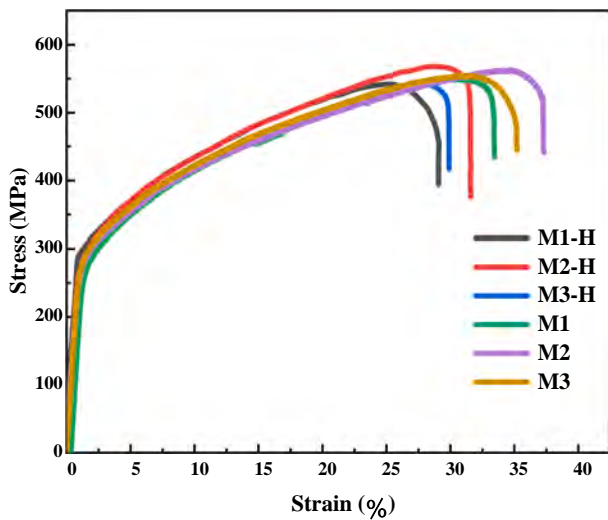**Fig. 8.** Variation of hydrogen concentration at points A and B.

Fig. 9. Stress–strain curves of M1, M2 and M3.

Table 6
Mechanical property of the welds.

Specimen		UTS(MPa)	El$_t$(%)	RA(%)	RA$_{loss}$(%)
M1	uncharged	552	35.1	51.7	34.6
	hydrogen-charged	543	29.1	33.8	
M2	uncharged	569	36.4	57.3	30.7
	hydrogen-charged	558	31.6	39.7	
M3	uncharged	553	35.3	52.7	33.2
	hydrogen-charged	542	29.9	35.2	

effect of the ferrite content on HE can be neglected. Therefore, it can be inferred that the difference in resistance to HE of M1, M2 and M3 stems from the different ferrite morphology in the welds. Studies [17,26,43,44] have shown that hydrogen-induced cracks and secondary cracks usually occur at the ferrite/austenite interface and consequently, hydrogen segregation at the interface exacerbates HE of the weld. As shown in Fig. 9 and Table 6, the order of the decreasing resistance to HE is skeletal ferrite, reticular ferrite and lathy ferrite which corresponds to the order of the increasing hydrogen segregation and confirms that ferrite morphology affects the resistance to HE of welds due to different hydrogen segregation at the ferrite/austenite interface. In addition, similar ferrite morphological dependence is observed from the fractures of the welds. Since the severe hydrogen segregation regions in M1 can form multiple crack nucleation positions during fracture, a wide range of cleavage zones composed of small cleavage facets are observed macroscopically from the fracture edge of M1. On account of the continuous structure of ferrite in M2 and M3, the cracks expand along the interface after initiation resulting in intergranular fracture macroscopically.

5. Conclusions

In this study, SKPFM, MFM and FEM are performed to investigate the effect of ferrite morphology on hydrogen distribution in the welds. Furthermore, microstructural characterization, SSRT test and fracture analysis are conducted to explore the relationship between ferrite morphology and HE. The conclusions are as follows:

(1) The ferrite/austenite interface becomes the hydrogen segregation region. Moreover, the degree of hydrogen segregation at the ferrite/austenite interface is affected by the ferrite morphology and shows the order of lathy ferrite > reticular ferrite > skeletal ferrite.

(2) The HE susceptibility of the weld containing lathy ferrite, skeletal ferrite and reticular ferrite is 34.6%, 30.7% and 33.2%, respectively. The resistance to HE shows the order of skeletal ferrite > reticular ferrite > lathy ferrite.
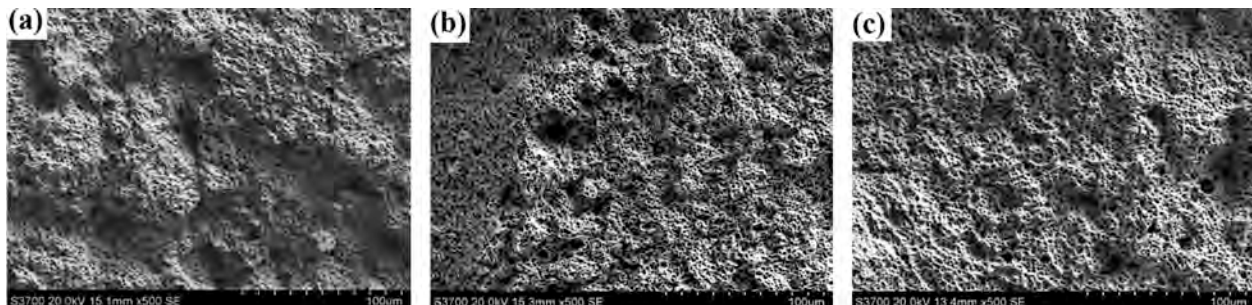

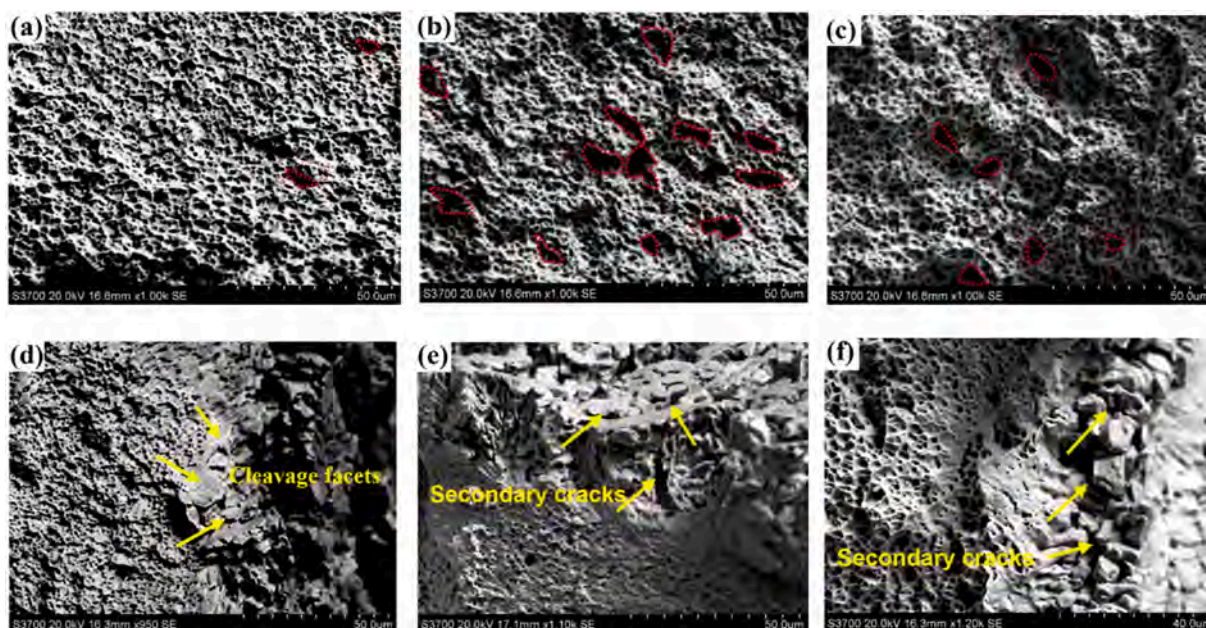**Fig. 10.** SEM micrographs of uncharged specimens: (a) M1, (b) M2, (c) M3.

Fig. 11. SEM micrographs of hydrogen-charged specimens: (a) Fracture center in M1, (b) Fracture center in M2, (c) Fracture center in M3, (d) Fracture edge in M1, (e) Fracture edge in M2, (f) Fracture edge in M3.

(3) The order of the decreasing HE resistance corresponds to the order of the increasing hydrogen segregation at the interface, indicating that the ferrite morphology influences the resistance to HE of the welds by affecting hydrogen segregation at the ferrite/austenite interface in welds.

(4) Similar ferrite morphological dependence is observed from the fracture of welds. The fracture of the weld containing lathy ferrite exhibits cleavage fracture, whereas the fracture of the weld containing reticular ferrite and the weld containing skeletal ferrite show intergranular fracture.

CRediT authorship contribution statement

Chilou Zhou: Investigation, Conceptualization, Methodology, Formal analysis, Data curation, Funding acquisition, Writing – original draft, Writing – review & editing, Supervision. **Pengzhi Dai:** Conceptualization, Methodology, Data curation, Writing – original draft, Writing – review & editing. **Hao Wu:** Methodology, Formal analysis, Writing – original draft. **Mohan He:** Data curation. **Xianhui Liu:** Data curation. **Paul K. Chu:** Writing – original draft, Funding acquisition.

Declaration of Competing Interest

The authors declare that they have no known competing financial interests or personal relationships that could have appeared to influence the work reported in this paper.

Acknowledgments

References

[1] J. Shang, Z. Hua, Hydrogen distribution and segregation in hydrogen-charged S30408 after fracture analyzed via scanning Kelvin probe force microscopy, Appl. Surf. Sci. 528 (2020), 147050.

[2] C. Zhou, X. Liu, Y. Zhang, H. Wu, Y. Yang, Numerical study on effect of inclusions on hydrogen segregation in steel under stress conditions, Int. J. Hydrogen Energy 47 (2022) 20310–20322.

[3] Y. Zheng, Y. Tan, C. Zhou, G. Chen, J. Li, Y. Liu, B. Liao, G. Zhang, A review on effect of hydrogen on rubber seals used in the high-pressure hydrogen infrastructure, Int. J. Hydrogen Energy 45 (2020) 23721–23738.

[4] S. Zhang, J. Li, T. An, S. Zheng, K. Yang, L. Lv, C. Xie, L. Chen, L. Zhang, Investigating the influence mechanism of hydrogen partial pressure on fracture toughness and fatigue life by in-situ hydrogen permeation, Int. J. Hydrogen Energy 46 (2021) 20621–20629.

[5] S. Zheng, L. Chen, C. Chen, Failure analysis of an A333Gr6 pipeline after exposure to a hydrogen sulfide environment, Eng. Fail. Anal. 35 (2013) 516–523.

[6] H.-Y. Zhang, J. Hu, X.-M. Meng, Y. Sun, T. Wang, W.-J. Lv, Q.-X. Shi, J.-Y. Ma, D.-Y. Zhou, W. Liang, L.-W. Zheng, Effect of deformation microstructures on hydrogen embrittlement sensitivity and failure mechanism of 304 austenitic stainless steel: the significant role of rolling temperature, J. Mater. Res. Technol. 17 (2022) 2831–2846.

[7] A. Laureys, T. Depover, K. Verbeken, Effect of environmental and internal hydrogen on the hydrogen assisted cracking behavior of TRIP-assisted steel, Mater. Sci. Eng., A 739 (2019) 437–444.

[8] Z. Hua, B. An, T. Iijima, C. Gu, J. Zheng, The finding of crystallographic orientation dependence of hydrogen diffusion in austenitic stainless steel by scanning Kelvin probe force microscopy, Scr. Mater. 131 (2017) 47–50.

[9] Z. Hua, D. Wang, Z. Liu, Y. Zhang, S. Zhu, Hydrogen distribution at twin boundary in austenitic stainless steel studied by scanning Kelvin probe force microscopy, Mater. Lett. 234 (2019) 175–178.

[10] L. Zhang, Z. Li, J. Zheng, Y. Zhao, P. Xu, C. Zhou, C. Zhou, X. Chen, Dependence of hydrogen embrittlement on hydrogen in the surface layer in type 304 stainless steel, Int. J. Hydrogen Energy 39 (2014) 20578–20584.

[11] S.R. Kumar, A.K. Singh, S. Sandeep, P. Aravind, Investigation on Microstructural behavior and Mechanical Properties of plasma arc welded dissimilar butt joint of austenitic- ferritic stainless steels, Mater. Today:. Proc. 5 (2018) 8008–8015.

[12] J. Li, H. Li, Y.u. Liang, P. Liu, L. Yang, Y. Wang, Effects of heat input and cooling rate during welding on intergranular corrosion behavior of high nitrogen austenitic stainless steel welded joints, Corros. Sci. 166 (2020) 108445, https://doi.org/ 10.1016/j.corsci.2020.108445.

[13] B. Gülenç, K. Develi, N. Kahraman, A. Durgutlu, Experimental study of the effect of hydrogen in argon as a shielding gas in MIG welding of austenitic stainless steel, Int. J. Hydrogen Energy 30 (2005) 1475–1481.

[14] X. Li, B. Gong, C. Deng, Y. Li, Effect of pre-strain on microstructure and hydrogen embrittlement of K-TIG welded austenitic stainless steel, Corros. Sci. 149 (2019) 1–17.

[15] Z.H. Fu, B.J. Yang, M.L. Shan, T. Li, Z.Y. Zhu, C.P. Ma, X. Zhang, G.Q. Gou, Z.R. Wang, W. Gao, Hydrogen embrittlement behavior of SUS301L-MT stainless steel laser-arc hybrid welded joint localized zones, Corros. Sci. 164 (2020), 108337.

[16] M. Landowski, A. Świerczyńska, G. Rogalski, D. Fydrych, Autogenous Fiber Laser Welding of 316L Austenitic and 2304 Lean Duplex Stainless Steels, Materials 13 (13) (2020) 2930, https://doi.org/10.3390/ma13132930.

[17] C.M. Younes, A.M. Steele, J.A. Nicholson, C.J. Barnett, Influence of hydrogen content on the tensile properties and fracture of austenitic stainless steel welds, Int. J. Hydrogen Energy 38 (2013) 4864–4876.

[18] L.W. Tsay, Y.C. Liu, M.C. Young, D.Y. Lin, Fatigue crack growth of AISI 304 stainless steel welds in air and hydrogen, Mater. Sci. Eng., A 374 (2004) 204–210.

[19] X. Li, B. Gong, C. Deng, Y. Li, Failure mechanism transition of hydrogen embrittlement in AISI 304 K-TIG weld metal under tensile loading, Corros. Sci. 130 (2018) 241–251.

[20] X. Li, B. Gong, X. Liu, C. Deng, Y. Li, Effects of hydrogen and microstructure on tensile properties and failure mechanism of 304L K-TIG welded joint, Mater. Sci. Eng., A 735 (2018) 208–217.

[21] J. Li, H. Li, W. Peng, T. Xiang, Z. Xu, J. Yang, Effect of simulated welding thermal cycles on microstructure and mechanical properties of coarse-grain heat-affected zone of high nitrogen austenitic stainless steel, Mater. Charact. 149 (2019) 206–217.

[22] A. Świerczyńska, D. Fydrych, M. Landowski, G. Rogalski, J. Łabanowski, Hydrogen embrittlement of X2CrNiMoCuN25-6-3 super duplex stainless steel welded joints under cathodic protection, Constr. Build. Mater. 238 (2020) 117697, https://doi.org/10.1016/j.conbuildmat.2019.117697.

[23] A.D. Rossin, T.H. Blewitt, A.R. Troiano, Hydrogen embrittlement in irradiated steels, Nucl. Eng. Des. 4 (5) (1966) 446–458.

[24] C.D. Beachem, A new model for hydrogen-assisted cracking (hydrogen "embrittlement"), Metall. Mater. Trans. B 3 (1972) 441–455.

[25] S. Lynch, Hydrogen embrittlement phenomena and mechanisms, Corros. Rev. 30 (2012) 105–123.

[26] M.i. Luppo, A. Hazarabedian, J. Ovejero-García, Effects of delta ferrite on hydrogen embrittlement of austenitic stainless steel welds, Corros. Sci. 41 (1999) 87–103.

[27] J.A. Brooks, A.J. West, Hydrogen induced ductility losses in austenitic stainless steel welds, Metall. Trans. A 12 (1981) 213–223.

[28] W. Chuaiphan, L. Srijaroenpramong, Effect of welding speed on microstructures, mechanical properties and corrosion behavior of GTA-welded AISI 201 stainless steel sheets, J. Mater. Process. Technol. 214 (2014) 402–408.

[29] ISO/TR 17671-1, Welding-Recommendations for welding of metallic materials-Part 1: General guidance for arc welding, International Organization for Standardization, 2002.

[30] EN 1011-1, Welding-Recommendations for welding of metallic materials- Part 1: General guidance for arc welding, European Committee for Standardization, 2009.

[31] H. Takegami, T. Shinoda, T. Saito, R.I. keo, Y. Kikuchi, Friction welding of pipe to plate: estimate of heat input and comparison with MAG welding, Weld. Int. 18 (6) (2004) 444–449.

[32] S. Ali Amin Alrabii, S. Sabeeh Abed-Alkarem, Study the Effect of CO2 Mag Welding Process Parameters on the Heat Input and Joint Geometry Dimensions Using Experimental and Computational Methods, Diyala Journal of, Eng. Sci. 8 (2) (2015) 47–71.

[33] M. Görkem, H. Efe, V. Onar, Microstructure analysis of XAR steel plate welded by mag welding method using different welding currents, Ejons Int. J. Math. Eng. Nat. Sci. 8 (2019) 22–29.

[34] G. Wang, Y.u. Yan, X. Yang, J. Li, L. Qiao, Investigation of hydrogen evolution and enrichment by scanning Kelvin probe force microscopy, Electrochem. Commun. 35 (2013) 100–103.

[35] A.O. Magne, O. Vigdis, Effect of Microstructure and Temperature on HydrogenDiffusion and Trapping in X70 grade Pipeline Steel and itsWeldments, proc spie, (2010).

[36] E. Owczarek, T. Zakroczymski, Hydrogen transport in a duplex stainless steel, Acta Mater. 48 (2000) 3059–3070.

[37] T. Fujii, T. Hazama, H. Nakajima, R. Horita, A safety analysis on overlay disbonding of pressure vessels for hydrogen service, Am. Soc. Met. (1982) 361–368.

[38] D.J. Kotecki, WRC-1992 Constitution Diagram for Stainless Steel Weld Metals, Welding J. 71 (1992).

[39] G. Mohammed, M. Ishak, S. Aqida, H. Abdulhadi, Effects of Heat Input on Microstructure, Corrosion and Mechanical Characteristics of Welded Austenitic and Duplex Stainless Steels: A Review, Metals 7 (2017).

[40] A. Głowacka, W.A. Świątnicki, Effect of hydrogen charging on the microstructure of duplex stainless steel, J. Alloy. Compd. 356–357 (2003) 701–704.

[41] R.J. Behm, K. Christmann, G. Ertl, Adsorption of hydrogen on Pd(100), Surf. Sci. 99 (1980) 320–340.

[42] M.G. Cattania, V. Penka, R.J. Behm, K. Christmann, G. Ertl, Interaction of hydrogen with a palladium (110) surface, Surf. Sci. 126 (1983) 382–391.

[43] B.S. Rho, H.U. Hong, S.W. Nam, The fatigue crack initiation at the interface between matrix and δ-ferrite in 304L stainless steel, Scr. Mater. 39 (1998) 1407–1412.

[44] M. Akita, M. Nakajima, K. Tokaji, Fatigue Behavior of Stainless Steels with Different Ferrite and Austenite Volume Fraction in 3%NaCl Solution, Tetsu-to-Hagane 89 (2009) 863–870.